

# Models of $(\text{ZrO}_2)_n$ Complexes Intercalated into Montmorillonite

Dmitrii Efremov,\* Tatyana Kuznetsova, Vladimir Doronin, and Vladislav Sadykov

Boreskov Institute of Catalysis, pr. Lavrentieva, 5, 630090 Novosibirsk, Russia

Received: October 27, 2004; In Final Form: February 17, 2005

The article discusses the properties of several model zirconium dioxide complexes  $(\text{ZrO}_2)_n$  intercalated into the interlayer space of montmorillonite clay. Grand canonical Monte Carlo simulation was used in a series of numerical experiments during analysis of the low-temperature nitrogen adsorption in the micropores thus generated. The goal of such experiments was to determine the geometrical parameters of introduced molecular complexes of different types inside micropores of various widths. The obtained information was used to characterize textural and structural properties of three pillared interlayer materials prepared by using pillaring species synthesized via aging of zirconyl chloride solutions containing as additives chlorides of Ca, Sr, or Ba. It was found that in the cases of Ba and Ca the interlayer micropores are filled with isolated tetramers  $(\text{ZrO}_2)_4$ . Meanwhile, the presence of Sr in the pillaring solution, most likely, favors the preservation of larger sheetlike complexes  $(\text{ZrO}_2)_8$ .

## Introduction

In the past few years, continuously growing attention of researchers is attracted to a relatively new class of microporous materials, pillared interlayer materials (PIMs), due to their reasonable thermal stability<sup>1</sup> and the excellent molecular sieve properties of their quasi-two-dimensional pore structure. For instance, clays pillared with nanosize zirconia particles are promising supports and catalysts for different petrochemical processes<sup>2</sup> and selective catalytic reduction of  $\text{NO}_x$  with hydrocarbons in excess of oxygen.<sup>3–6</sup> Besides, PIMs are promising materials for purification and storage of natural gas.<sup>7–9</sup>

However, despite numerous potential applications and the existence of a great number of experimental data, very few papers are devoted to detailed investigation of the PIM pore structure by adsorption methods. Thereupon, it is necessary to note that in the majority of papers dealing with characterization of the PIM pore structure by adsorption methods or devoted to simulation of adsorption in PIM micropores, pillared (nano)-particles (PP) inside the micropores are modeled either as cylindrical columns with rectangular or round cross section<sup>10–12</sup> or as vertical chains of Lennard-Jones spherical molecules.<sup>13–16</sup> Meanwhile, there is no reliable proof in the literature that such a simplified approach to molecular geometry of pillars does not significantly affect analysis of the PIM adsorption properties, especially when their concentration in the interlayer micropores (galleries) is high.

The goal of the current paper was to test the effect of various parameters of model pillars on characteristics of the pore structure of three distinct PIM samples using computer simulation of nitrogen adsorption at 77 K by grand canonical Monte Carlo (GCMC) with a due regard for the X-ray diffraction (XRD) information on the molecular geometry of different polycations  $[\text{Zr}_4(\text{OH})_8(\text{H}_2\text{O})_{16}]_n$  pillared from solution into the montmorillonite interlayer space.

## Experimental Section

Zirconia-pillared clays were synthesized using a Ca-montmorillonite clay from the Kazakhstan deposit containing 66 wt

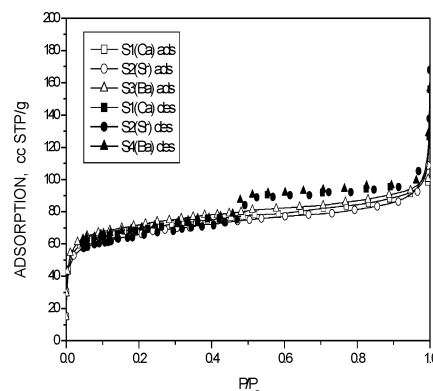


**Figure 1.** Isotherms of nitrogen adsorption and desorption at  $T = 77.4$  K over PIM samples S1(Ca), S2(Sr), and S3(Ba).

%  $\text{SiO}_2$  and 25 wt %  $\text{Al}_2\text{O}_3$  following earlier described procedures.<sup>4</sup> Pillaring Zr-containing solutions were prepared from recrystallized  $\text{ZrOCl}_2 \cdot 8\text{H}_2\text{O}$  with addition of Ca, Sr, and Ba chlorides. Other details on the preparation and characterization of the pillaring solutions can be found in the paper of Sadykov et al.<sup>6</sup>

The chemical composition of Zr-PIM samples was analyzed by atomic absorption spectroscopy using a Karl Zeiss Jena AAS1N spectrometer.

The structure of nanopillars after the montmorillonite clay pillaring was studied previously by applying X-ray structural analysis, wide-angle X-ray scattering (WAXS) and extended X-ray absorption fine structure (EXAFS).<sup>5,6,17</sup>

Nitrogen adsorption isotherms for all three materials were measured at 77 K to obtain information on the specific micropore volume and specific surface area of mesopores. The isotherms presented in Figure 1 were measured in the relative pressure range  $0.002 < P/P_s < 1$  using an automatic adsorption installation Sorptomatic 1900. The isotherms in the low- and super-low-pressure range ( $10^{-6} < P/P_s < 0.1$ ) were refined using an adsorption installation ASAP 2010.

Some characteristics of the pore structure of studied samples based upon routine analysis of adsorption and XRD data are

**TABLE 1: Experimental Data for Samples S1(Ca), S2(Sr), and S3(Ba)**

sample	wt fraction of pillars, $X$	wt fraction of modifier	$d_{001}$ (XRD), nm	$A_{\text{ext}}$ , m <sup>2</sup> /g	$V_{\text{mic}}$ ( $\alpha_s$ -plot), cm <sup>3</sup> /g	$V_{\text{mic}}$ (TOZM), cm <sup>3</sup> /g	$A_{\text{os}}$ , m <sup>2</sup> /g	$A_{\text{BET}}$ , m <sup>2</sup> /g	$A_{0\Sigma}$ , m <sup>2</sup> /g	$V_{0\Sigma}$ , cm <sup>3</sup> /g
S1(Ca)	0.200	0.002 Ca	1.74	80.0	0.073	0.173	794	249	635	0.254
S2(Sr)	0.195	0.002 Sr	1.77	98.6	0.060	0.162	810	236	639	0.265
S3(Ba)	0.206	0.002 Ba	1.87	94.8	0.071	0.154	789	257	630	0.293

summarized in Table 1. These samples are referred to as S1-(Ca), S2(Sr), and S3(Ba), where symbols in parentheses are related to cations added to pillaring solutions. The meaning of  $d_{001}$  in the 4th column of Table 1 is clear from Figure 2. The sizes of the corresponding interlayer galleries were found by subtracting the crystallographic thickness of one montmorillonite layer from  $d_{001}$ :

$$H_p = d_{001} - d_{001}^0 \quad (1)$$

where  $d_{001}^0 = 0.94 \text{ nm}$ .<sup>10–11</sup>

The values of the relative mesopore surface area  $A_{\text{ext}}$  in the 5th column of Table 1 and micropore volume  $V_{\text{mic}}$  in the 6th column of Table 1 were found using the  $\alpha_s$ -plot<sup>18</sup> in the relative pressure range  $0.1 < P/P_s < 0.38$ . The  $A_{\text{os}}$  value in the 8th column was also found using the  $\alpha_s$ -plot but at much lower pressures than in the case of  $A_{\text{ext}}$ . According to some researchers, this value has the meaning of the total specific surface area of micro- and mesopores (see, e.g., ref 19). In the present paper we attempted to calculate the  $A_{\text{os}}$  values in the range  $10^{-4} < P/P_s < 10^{-2}$  on the basis of the following expression for the universal  $t$ -curve:

$$t \text{ (nm)} = 0.1 \left[ \frac{6.5569}{0.8756 - \lg(P/P_s)} \right]^{1.023}$$

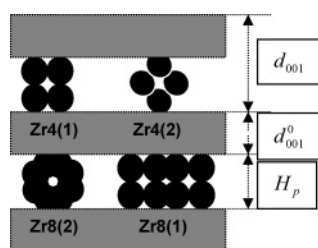
The use of this expression allows one to achieve an excellent agreement with the reference isotherm<sup>18</sup> at  $P/P_s < 0.4$  in terms of the smallest mean-square deviation. Specific surface area  $A_{\text{BET}}$  (column 9) was determined in the range  $0.001 < P/P_s < 0.2$  because the best correlation of the Brunauer–Emmett–Teller (BET) plot with the experimental data was achieved in this range. The total micropore volume in the 7th column of Table 1 was determined using the well-known Dubinin–Radushkevich equation in the range  $0.001 < P/P_s < 0.15$ . The  $A_{0\Sigma}$  value in the next to last column in Table 1 was introduced by Derevyankin et al.<sup>10</sup> for the case of the partially ordered PIM model to calculate the ordering degree in the structure of real PIM. Let  $X$  be the weight fraction of pillars (see the 2nd column of Table 1). Then  $A_{0\Sigma}$  may be found from

$$A_{0\Sigma} = A_{0\Sigma}^*(1 - X) \quad (2)$$

where

$$A_{0\Sigma}^* = 2abN_A/M_U \quad (3)$$

This is the theoretical maximum of the specific surface area of

**Figure 2.** Model complexes  $(\text{ZrO}_2)_n$  in the montmorillonite micropores.**TABLE 2: Parameters of Potential Models for Nitrogen, Pillar, and Layered Walls**

$\text{N}_2$		pillar		layered wall	
$\sigma_{\text{ff}}$ , nm	$\epsilon_{\text{ff}}/k$ , K	$\sigma_{\text{pp}}$ , nm	$\epsilon_{\text{pp}}/k$ , K	$\sigma_{\text{ww}}$ , nm	$\epsilon_{\text{ww}}/k$ , K
0.394	96.02	0.352	28.0	0.34	28.0

the initial clay. This maximum is achieved in the case of the host crystal splitting into separate lamellae. Using expression 2, we assumed the montmorillonite elementary cell to have molecular weight  $M_U = 747.1 \text{ g/mol}$  and rectangular bases with sides  $a = 0.53 \text{ nm}$  and  $b = 0.93 \text{ nm}$ .<sup>10,11</sup> From eqs 1 and 2, it is easy to calculate the maximum theoretical volume of micropores in montmorillonite (assuming ideal PIM ordering):

$$V_{0\Sigma} = 0.5H_p A_{0\Sigma} = 0.5(d_{001} - d_{001}^0)A_{0\Sigma} \quad (4)$$

The distance between the boundary layers of oxygen ions for a given montmorillonite sheet,  $d_{001}^0$ , was taken as  $0.94 \text{ nm}$ .<sup>10,11</sup> Let us finish this section with the expression for the fraction of ordered regions in a PIM structure<sup>10</sup> that we shall need below (section 4).

$$\zeta = \frac{A_0}{A_{0\Sigma} - A_{\text{ex}}} = \frac{V_m + V_F}{V_{0\Sigma}} \quad (5)$$

Here  $A_0$  is the theoretical surface area of galleries in the ordered part of the PIM that can be obtained by mental removal of all pillars,  $V_F$  is the volume occupied by pillars, and  $V_m$  is the remaining accessible volume of interlayer micropores in the same ordered part of the PIM.

### Description of Model Pillars in Montmorillonite Interlayer Micropores

**Molecular Geometry of Pillars.** In our simulations we have considered 4 variants of model pillars  $(\text{ZrO}_2)_n$  that, according to available data,<sup>17,20</sup> may be present in montmorillonite micropores after the final thermal treatment. First of all, this is the simplest tetramer  $(\text{ZrO}_2)_4$  that was simplistically dealt as a square with  $0.35 \text{ nm}$  sides. Effective Lennard-Jones (LJ) centers with potential parameters listed in Table 2 were located at the vertexes of the square. It was assumed that this tetramer could have two orientations in a model micropore ( $\text{Zr}4(1)$  and  $\text{Zr}4(2)$  in the top part of Figure 2). Preservation of the basic zirconium tetramer unit structure in Zr-pillared clays such as montmorillonite<sup>17</sup> or beidellite<sup>20</sup> was reliably proved by using EXAFS<sup>17,20</sup> and WAXS<sup>17</sup> data. In addition to tetramers, more bulky Zr polycations are known to exist in pillaring solutions.<sup>17,21–24</sup> As revealed by small-angle X-ray scattering (SAXS),<sup>17,21,23</sup> these species have either sheetlike or rodlike shape as dependent upon the exact composition of pillaring solutions and their aging conditions. Thus, for Ca- or Ba-containing pillaring solutions, nanorods comprised of 2 stacked tetramers dominate, while Sr addition helps to stabilize sheetlike structures as well.<sup>17,23</sup> In solution, these species appear to be stabilized against further polymerization by alkaline-earth cations situated both between and outside the tetrameric units being coordinated to terminal and/or bridging hydroxyls. After pillaring and washing of a clay,

all alkaline-earth cations are removed from the sample.<sup>6,17,23</sup> This suggests that the molecular configuration of the zirconia nanoparticles could differ considerably from that of pillaring species in solutions. Hence, to verify by simulation of the nitrogen adsorption isotherms which type of pillars could be present in washed and calcined pillared clays, two types of Zr<sub>8</sub> complexes were considered. The first one denoted as Zr8(1) (Figure 2) consists of two tetramers stacked side by side in a planar configuration. Here, each pair of Zr cations belonging to different tetramers and situated at a distance of ca. 0.3 nm is bound by two bridging hydroxyls. Hence, this structure is inscribed into a 1 nm × 0.35 nm rectangle.<sup>21</sup>

Another Zr<sub>8</sub> configuration found for pillaring species in solutions consists of two tetramers stacked on top of each other attaching themselves with four single OH<sup>−</sup> bridges.<sup>17,21,22</sup> In this case, exact distance between tetramers can exceed the minimum value of 0.3 nm<sup>21</sup> due to a weaker bonding and considerable distortion of the tetramer structure especially when stabilizing alkaline-earth cations are incorporated between tetramers.<sup>17,21</sup> After fixation of these complexes in the interlayer galleries due to interaction with aluminosilicate layers, enlarged distances between tetramers in pillars could be preserved despite subsequent removal of stabilizing cations by washing. From the simulation point of view, the most essential difference between the sheetlike and nanorod-like structure of pillars is that in the latter case N<sub>2</sub> molecules could not enter the space between the tetramers provided they are situated at a distance of less than 1 nm. This is due to a screening of the intertetrameric space by bridging hydroxyls connecting Zr cations. Hence, as a simplest limiting case reflecting the specificity of the nanorods' effect on the nitrogen adsorption isotherms, the distance between tetramers lying in parallel planes (Figure 2, Zr8(2) complex) was chosen to be equal to 1 nm (±20%). As suggested in refs 17 and 21, to minimize the electrostatic repulsion between Zr cations, tetramers were rotated for 45° relative each other. Certainly, more bulky nanorods could be present in pillaring solutions<sup>17,21,24</sup> as directly revealed by transmission electron microscopy after their clustering into colloidal aggregates,<sup>22</sup> and they could be pillared into clays as well.<sup>24</sup> However, qualitatively their effect of blocking the gallery space for nitrogen adsorption will be the same as for model Zr8(2) complexes. Moreover, in studied cases, pillared clays were prepared by using solutions in which the content of such big complexes was minimized by tuning the composition of solutions and their aging conditions.<sup>17,22</sup> From a simulation point of view, realization of appropriate GCMC experiments for bigger complexes would meet some complications and uncertainties (vide infra), which could require too expensive work without achieving any noticeable improvement in simulation.

**Potential Models.** In GCMC simulations, the total potential energy  $\Phi_{\text{tot}}$  of adsorbate molecules confined in layered pillared pores is a sum of three energies: potential energy between the molecules of adsorbed fluid,  $\Phi_{\text{ff}}$ , potential energy between the fluid molecules and PP,  $\Phi_{\text{fp}}$ , and potential energy between the adsorbate molecules and the pore walls,  $\Phi_{\text{fw}}$ :

$$\Phi_{\text{tot}} = \Phi_{\text{ff}} + \Phi_{\text{fw}} + \Phi_{\text{fp}}$$

In this expression the interaction of the fluid molecules is described by cut and shifted LJ potential<sup>25</sup>

$$\Phi_{\text{ff}} = \begin{cases} \Phi_{\text{LJ}}(r) - \Phi_{\text{LJ}}(r_c), & r < r_c \\ 0, & r \geq r_c \end{cases}$$

where  $r$  is the intermolecular distance,  $r_c$  is the cutoff radius,  $r_c$

$= 5\sigma_{\text{ff}}$ , and  $\Phi_{\text{LJ}}$  is the full LJ potential,

$$\Phi_{\text{LJ}}(r) = 4\epsilon_{\text{ff}} \left[ \left( \frac{\sigma_{\text{ff}}}{r} \right)^{12} - \left( \frac{\sigma_{\text{ff}}}{r} \right)^6 \right]$$

where  $\epsilon_{\text{ff}}$  and  $\sigma_{\text{ff}}$  are the energy and size parameters of the fluid molecules.

Assuming that PP are composed from  $N_p$  LJ centers with atomic size  $\sigma_{\text{pp}}$ , the site-to-site method is used to calculate the interaction between the fluid molecules and the pillars,

$$\Phi_{\text{fp}} = \sum_{i=1}^{N_f} \sum_{j=1}^{nN_p} \left[ \left( \frac{\sigma_{\text{fp}}}{r_{ij}} \right)^{12} - \left( \frac{\sigma_{\text{fp}}}{r_{ij}} \right)^6 \right]$$

where  $N_f$  is the number of adsorbate molecules in the simulation box,  $n$  is the number of LJ centers in one PP,  $r_{ij}$  is the intermolecular distance between a fluid molecule and an atom of the pillars, and  $\epsilon_{\text{fp}}$  and  $\sigma_{\text{fp}}$  are the cross energy and size parameter, which are obtained from the Lorentz–Berthelot (LB) combining rules.

The interaction between a layered wall and a fluid molecule is represented by the well-known Steele 10–4–3 potential,<sup>26</sup>

$$\Phi_{\text{fw}} = 2\pi\rho_w\epsilon_{\text{fw}}\sigma_{\text{fw}}^2\Delta \left[ 0.4 \left( \frac{\sigma_{\text{fw}}}{z} \right)^{10} - \left( \frac{\sigma_{\text{fw}}}{z} \right)^4 - \left( \frac{\sigma_{\text{fw}}^4}{3\Delta(0.61\Delta + z)^3} \right) \right]$$

where  $\rho_w$  is the density of the solid wall,  $\rho_w = 114 \text{ nm}^{-3}$ ,  $\Delta = 0.335 \text{ nm}$ ,  $z$  is the normal distance between an adsorbate molecule and one of the solid walls, and  $\epsilon_{\text{fw}}$  and  $\sigma_{\text{fw}}$  are the cross interaction parameters, which are obtained from the modified LB combining rules,<sup>14</sup>

$$\epsilon_{\text{fw}} = k_{\text{fw}}(\epsilon_{\text{ff}}\epsilon_{\text{ww}})^{0.5} \quad \sigma_{\text{fw}} = 0.5(\sigma_{\text{ww}} + \sigma_{\text{ff}})$$

where additional term  $k_{\text{fw}}$  is the binary interaction parameter,  $k_{\text{fw}} = 0.65$ , which was found in ref 14 by fitting the simulation results to the appropriate experimental data. The energy and size parameters of the fluid molecule, the pillar atom, and the layered solid wall are listed in Table 2.

The values of  $\epsilon_{\text{ww}}$ ,  $\epsilon_{\text{pp}}$ ,  $\sigma_{\text{ww}}$ , and  $\sigma_{\text{pp}}$  were offered by Yi et al.<sup>15</sup> The energy parameter  $\epsilon_{\text{ff}}/k = 96.02 \text{ K}$  is slightly greater than well-known quantity 95.0 K.<sup>27,28</sup> The difference equal to 1.02 K was found for long-range energy corrections during special GCMC runs by analyzing the results for  $R_c = 5\sigma_{\text{ff}}$  and  $R_c = 10\sigma_{\text{ff}}$ . The size parameter  $\sigma_{\text{ff}}$  may be found from the agreement of the saturated vapor pressure of N<sub>2</sub> at 77.4 K<sup>29</sup> with the normalized vapor pressure of LJ liquid  $P_s\sigma_{\text{ff}}^3/\epsilon_{\text{ff}}$  at normalized temperature 77.4 K/ $\epsilon_{\text{ff}}$ .<sup>30</sup>

**Geometrical Characteristics of Model Pillars.** As the main goal of this work is the pore structure characterization by analysis of the nitrogen adsorption isotherms, it seems reasonable to determine the volume of each model pillar using the number of N<sub>2</sub> molecules displaced by one pillar located in an empty pore of a given size at the same pressure. Then, this number of molecules has to be multiplied by the volume occupied by one N<sub>2</sub> molecule in an empty pore. In accordance with the above, it is easy to determine the total area of the top and bottom pillar bases (or simply “area of bases”) using the difference between the number of molecules touching the walls of an empty pore and an analogous value for a pore with a pillar. Then, this difference has to be multiplied by the area occupied by one molecule in a pore without a pillar. The determination of the pillar side surface area appears to be somewhat less



straightforward. In GCMC simulations presented below, we calculated the average number of nitrogen molecules located no further than the equilibrium diameter of a nitrogen molecule  $d_{\text{ff}} = 2^{1/6}\sigma_{\text{ff}}$  from LJ centers of pillars and multiplied this value by 0.16 nm. In the case of Zr8(2), we also took into account nitrogen molecules with the centers located no further than the  $d_{\text{ff}}$  distance from the axis of this complex.

All GCMC simulations necessary for determination of the pillar geometrical characteristics were carried out using a common algorithm<sup>28,31</sup> in simulation boxes with  $10\sigma_{\text{ff}} \times 10\sigma_{\text{ff}}$  square bases. Their height was equal to 0.80, 0.83, and 0.93 nm in accordance with the height of interlayer galleries in the studied PIM (see Table 1 and eq 1). In 12 cases out of 15, one of the considered model pillar complexes was placed in the pore center. The results of numerical calculations are reported here for relative pressure  $P/P_s = 1$ . However, they are valid with a good accuracy for the interval  $0.1 < P/P_s < 1$ . The reported value of normalized activity  $Z\sigma_{\text{ff}}^3$  required for GCMC calculations was determined for a given pressure  $P$  (and temperature  $T$ ) using four virial coefficients for LJ gas as follows:

$$Z\sigma_{\text{ff}}^3 = \frac{P_{\text{id}}(P) \sigma_{\text{ff}}^3}{kT}$$

In this equation the ideal gas pressure  $P_{\text{id}}$  can be easily calculated numerically from the equation

$$P = P_{\text{id}}(1 + B_1 + B_2 + B_3 + B_4) \quad (6)$$

Here  $B_i$  values can be written in a common way as

$$B_i = (\Gamma - b_i)\rho^i$$

Dimensionless constants  $b_i$  have the following values:  $b_1 = -1.612468$ ,  $b_2 = 0.580848$ ,  $b_3 = 0.211070$ , and  $b_4 = 1.199669$ . All these parameters were fitted by us in such a way that provides the best description of virial coefficients for the LJ gas<sup>32</sup> in the range  $0.5 < kT/\epsilon_{\text{ff}} < 1.3$ .

$\Gamma$  and  $\rho$  values are defined as

$$\Gamma = - \left| \frac{kT}{\epsilon_{\text{ff}}} - 1.98445 \right|^{4.44373} \quad \rho = \frac{2\pi P_{\text{id}}\sigma_{\text{ff}}^3}{3kT}$$

Note that the easiest way to find the solution of eq 6 is by using the well-known bisection method in the pressure range ( $P$ , 1.14 $P$ ). At the discussed  $T$ ,  $\sigma_{\text{ff}}$ , and  $\epsilon_{\text{ff}}$  values, the nonideal pressure  $P = 1$  atm corresponds to the ideal pressure  $P_{\text{id}} = 1.05$  atm.

In all our simulations, the periodic boundary conditions were imposed in the lateral directions, and  $1.1 \times 10^8$  configurations were generated (the first  $10^7$  configurations were discarded to guarantee equilibration). So a large number of configurations was used because after the first  $5.1 \times 10^7$  MC trials some of the obtained PP characteristics appeared to be not obvious to us.

Figures 3 and 4 present the final momentary molecular configurations (snapshots) in pores with the size  $H_p = 0.93$  nm containing Zr8(2) and Zr8(1), respectively. The circles around the LJ centers of nitrogen molecules have the equilibrium radius  $d_{\text{ff}}/2$ . The dark figures in the center are pillars. One can see that the configuration of the nitrogen atoms is close to a hexagonally packed monolayer. Indeed, during numerical experiments in the pores of this width the  $z$ -coordinates of approximately 90% of the centers of  $\text{N}_2$  molecules did not deflect from  $H_p/2$  in the direction of the pore walls by more

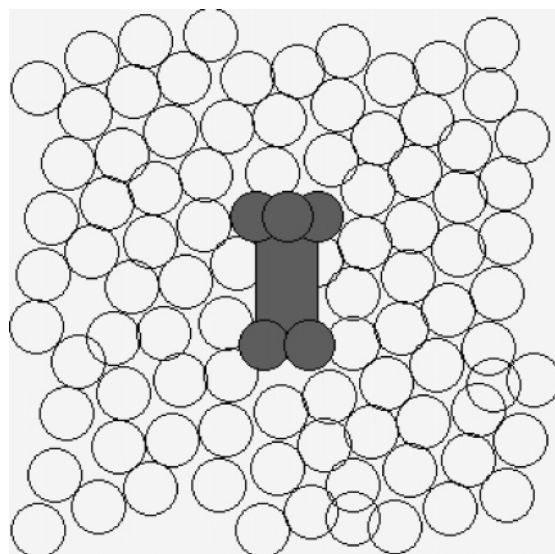


**Figure 3.** Snapshot of the final molecular configuration of nitrogen adsorbed at  $T = 77.4$  K and  $P/P_s = 1$  in a pore with width  $H_p = 0.93$  nm containing Zr8(2) complex (top view).

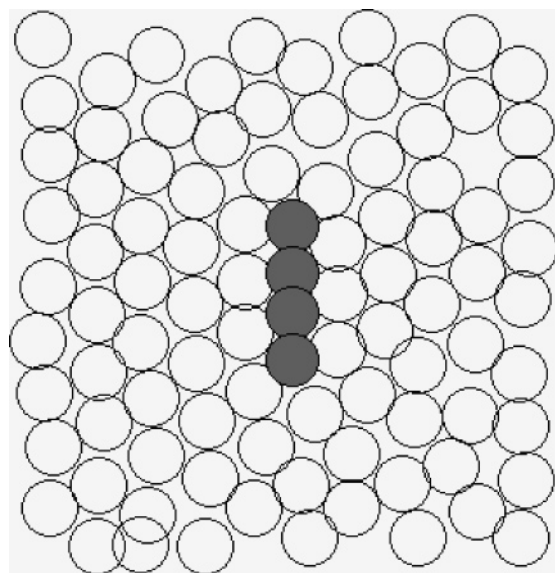


**Figure 4.** Snapshot of the final molecular configuration of nitrogen adsorbed at  $T = 77.4$  K and  $P/P_s = 1$  in a pore with width  $H_p = 0.93$  nm containing Zr8(1) complex (top view).

than  $0.05H_p$ . In smaller pores the corresponding deviations were even shorter. This observation led us to the conclusion that in the pores of studied dimensions nitrogen molecules (and, obviously, larger molecules) form a mobile two-dimensional structure.

The average numbers of all molecules,  $N_{\text{tot}}$ , which were determined in  $5 \times 10^8$  MC trials in each of 15 simulations for pore sizes 0.8, 0.83, and 0.93 nm, are listed in columns 2–4 of Table 3, respectively. The top rows with figures present these values for “empty” pores, i.e., pores without pillars. The subsequent rows contain these values for pores containing pillars indicated in the first column of Table 3.

The numbers of molecules with centers “touching” the pillar side surface,  $N_{\text{side}}$ , (see above) are reported in columns 5–7. Finally, the last three columns contain the numbers  $N_{\text{bi}}$  meaning the average numbers of molecules whose centers are located at distances shorter than  $d_{\text{ff}}$  from the pore walls. Obviously, we can calculate the effective geometrical volume of pillars by

**TABLE 3: Number of N<sub>2</sub> Molecules in Montmorillonite Galleries of Different Heights**

$V_{\text{box}} = 100\sigma_{\text{ff}}^2 \times H_p, \text{ nm}^3$	$N_{\text{tot}}$ for different pore heights			$N_{\text{side}}$ for different pore heights			$N_{\text{bot}}$ for different pore heights		
	$H_p = 0.80 \text{ nm}$	$H_p = 0.83 \text{ nm}$	$H_p = 0.93 \text{ nm}$	$H_p = 0.80 \text{ nm}$	$H_p = 0.83 \text{ nm}$	$H_p = 0.93 \text{ nm}$	$H_p = 0.80 \text{ nm}$	$H_p = 0.83 \text{ nm}$	$H_p = 0.93 \text{ nm}$
void pore	91.438	93.214	94.630				91.438	93.212	94.300
Zr4(1)	90.545	91.924	92.477	4.893	4.836	5.184	90.544	91.922	92.237
Zr4(2)	89.302	90.854	92.096	6.022	5.260	5.657	89.305	90.853	91.991
Zr8(1)	88.613	90.233	90.925	7.702	7.606	8.003	88.610	90.236	90.613
Zr8(2)	88.255	88.214	89.355	8.420	7.997	8.611	88.255	88.207	89.177

**TABLE 4: Volume, Side, and Top + Bottom Surface Areas of the Model (ZrO<sub>2</sub>)<sub>n</sub> Complexes**

$V_{\text{box}} = 100\sigma_{\text{ff}}^2 \times H_p, \text{ nm}^3$	volume of pillars for different pore heights, nm <sup>3</sup>			side surface area of pillars for different pore heights, nm <sup>2</sup>			sum of top and bottom area of pillars for different pore heights, nm <sup>2</sup>		
	$H_p = 0.80 \text{ nm}$	$H_p = 0.83 \text{ nm}$	$H_p = 0.93 \text{ nm}$	$H_p = 0.80 \text{ nm}$	$H_p = 0.83 \text{ nm}$	$H_p = 0.93 \text{ nm}$	$H_p = 0.80 \text{ nm}$	$H_p = 0.83 \text{ nm}$	$H_p = 0.93 \text{ nm}$
Zr4(1)	0.1215	0.1787	0.3291	0.1429	0.2064	0.3445	0.3038	0.4305	0.7078
Zr4(2)	0.2910	0.3269	0.3874	0.3421	0.3276	0.4054	0.7274	0.7877	0.8331
Zr8(1)	0.3845	0.4130	0.5664	0.4520	0.4770	0.5928	0.8612	0.9949	1.2181
Zr8(2)	0.4332	0.6925	0.8064	0.5093	0.8000	0.8440	1.0830	1.6688	1.7342

**TABLE 5: Calculated S1(Ca) Data**

$Zr_n(m)$	$V_{\text{mg}}, \text{ cm}^3/\text{g}$	$V_i, \text{ cm}^3/\text{g}$	$V_0, \text{ cm}^3/\text{g}$	$A_0, \text{ m}^2/\text{g}$	$A_+, A_-, \text{ m}^2/\text{g}$	$A_{\text{meas}}, \text{ m}^2/\text{g}$	$A_{\text{mic}}, \text{ m}^2/\text{g}$	$\rho_{\text{pp}}, \text{ g/cm}^3$	$\zeta$	$\epsilon_v, \epsilon_a$	$d_{\text{pv}}, d_{\text{pa}}, \text{ nm}$	$d_{\text{ipv}}, d_{\text{ipa}}, \text{ nm}$
Zr4(1)	0.173	0.030	0.203	443	48, 19	424	472	6.73	0.80	0.85, 0.96	0.440, 0.440	0.654, 1.605
Zr4(2)	0.173	0.071	0.244	533	59, 44	489	547	2.82	0.96	0.71, 0.92	0.680, 0.680	0.520, 1.564
Zr8(1)	0.173	0.047	0.220	481	151, 117	363	513	4.26	0.87	0.79, 0.76	0.783, 0.782	0.829, 0.724
Zr8(2)	0.173	0.053	0.226	493	165, 132	361	526	3.78	0.89	0.77, 0.73	0.830, 0.829	0.803, 0.697

**TABLE 6: Calculated S2(Sr) Data**

$Zr_n(m)$	$V_{\text{mg}}, \text{ cm}^3/\text{g}$	$V_i, \text{ cm}^3/\text{g}$	$V_0, \text{ cm}^3/\text{g}$	$A_0, \text{ m}^2/\text{g}$	$A_+, A_-, \text{ m}^2/\text{g}$	$A_{\text{meas}}, \text{ m}^2/\text{g}$	$A_{\text{mic}}, \text{ m}^2/\text{g}$	$\rho_{\text{pp}}, \text{ g/cm}^3$	$\zeta$	$\epsilon_v, \epsilon_a$	$d_{\text{pv}}, d_{\text{pa}}, \text{ nm}$	$d_{\text{ipv}}, d_{\text{ipa}}, \text{ nm}$
Zr4(1)	0.144	0.043	0.187	381	46, 26	355	401	4.58	0.70	0.77, 0.93	0.524, 0.524	0.521, 1.397
Zr4(2)	0.144	0.078	0.222	453	50, 47	406	456	2.50	0.84	0.65, 0.90	0.708, 0.707	0.431, 1.387
Zr8(1)	0.144	0.049	0.194	394	145, 119	276	421	3.96	0.73	0.75, 0.70	0.796, 0.796	0.707, 0.587
Zr8(2)	0.144	0.083	0.227	462	152, 199	264	416	2.36	0.85	0.64, 0.57	1.030, 1.030	0.596, 0.465

**TABLE 7: Calculated S3(Ba) Data**

$Zr_n(m)$	$V_{\text{mg}}, \text{ cm}^3/\text{g}$	$V_i, \text{ cm}^3/\text{g}$	$V_0, \text{ cm}^3/\text{g}$	$A_0, \text{ m}^2/\text{g}$	$A_+, A_-, \text{ m}^2/\text{g}$	$A_{\text{meas}}, \text{ m}^2/\text{g}$	$A_{\text{mic}}, \text{ m}^2/\text{g}$	$\rho_{\text{pp}}, \text{ g/cm}^3$	$\zeta$	$\epsilon_v, \epsilon_a$	$d_{\text{pv}}, d_{\text{pa}}, \text{ nm}$	$d_{\text{ipv}}, d_{\text{ipa}}, \text{ nm}$
Zr4(1)	0.188	0.083	0.271	496	52, 43	453	505	2.49	0.93	0.69, 0.91	0.671, 0.658	0.485, 1.474
Zr4(2)	0.188	0.097	0.286	523	57, 48	474	532	2.11	0.97	0.66, 0.91	0.728, 0.696	0.459, 1.493
Zr8(1)	0.188	0.071	0.260	475	161, 153	322	483	2.89	0.89	0.72, 0.68	0.881, 0.880	0.720, 0.595
Zr8(2)	0.188	0.101	0.290	530	173, 213	317	491	2.03	0.98	0.65, 0.60	1.051, 1.037	0.640, 0.521

subtracting  $N_{\text{tot}}(H_p, ZrN(m))$  for the corresponding pillar  $ZrN(m)$  from  $N_{\text{tot}}(H_p)$  for an empty pore and multiplying this difference by the volume occupied by a nitrogen molecule in an empty pore  $V_{\text{box}}(H_p)/N_{\text{tot}}(H_p)$ . To calculate the surface area of pore walls taken by PP from adsorbate molecules, it is necessary to subtract  $N_{\text{bt}}(H_p, ZrN(m))$  for the corresponding pillar  $ZrN(m)$  from  $N_{\text{bt}}(H_p)$  for an empty pore and divide the resulting difference by the surface area of a pore related to one adsorbate molecule in an empty pore,  $200\sigma_{\text{ff}}^2/N_{\text{bt}}(H_p, ZrN(m))$ .

Finally, the effective geometrical area of the pillar side surface was calculated by multiplying  $N_{\text{side}}$  by 0.16 nm. The results of all these calculations are reported in Table 4.

## Results and Discussion

Using the data of Tables 1 and 4, it is easy to make a detailed analysis of the micropore structure and macrotecture of studied samples in the frames of the partially disordered PIM model.<sup>10</sup> Tables 5–7 contain all necessary results for samples S1(Ca), S2(Sr), and S3(B), correspondingly, for each of the four pillar models considered above. The value  $V_{\text{mg}}$  in the second column of Tables 5–7 means the true specific geometrical micropore

volume. To determine this value, it is necessary to remember that when the micropore volume is calculated using the  $\alpha_s$ -method it is assumed that each adsorbate molecule occupies the same volume in the micropores as in the bulk liquid. Therefore, to pass from  $V_m$  ( $\alpha_s$ -plot) values from Table 1 to specific geometrical volume  $V_{\text{mg}}$ , it is necessary to use the ratio of the volume occupied by one N<sub>2</sub> molecule in the interlayer micropore ( $v_{\text{sl}} = V_{\text{box}}/N_{\text{tot}}$ , see previous section) to the volume occupied in the bulk of liquid nitrogen ( $v_l = v_{\text{mol}}/N_a$ , where  $v_{\text{mol}} = 34.68 \text{ cm}^3/\text{g}$  is the molar volume of liquid nitrogen at 77 K, and  $N_a$  is the Avogadro number),

$$V_{\text{mg}} = \frac{v_{\text{sl}}}{v_l} V_m (\alpha_s\text{-plot})$$

Note that  $V_{\text{mg}}$  values reported in Tables 5–7 are in good correlation with  $V_m$  (TOZM) values from Table 1 calculated using the Dubinin–Radushkevich equation, especially for the sample S1(Ca).

The densities of each pillar in a gallery of the corresponding height,  $\rho_{\text{pp}}$  (see columns 9 in Tables 5–7), were calculated using

pillar volumes (see columns 2–4 in Table 4):

$$\rho_{pp} = M_{pp}/V_{pp}$$

Here  $M_{pp} = n \times 2.0462 \times 10^{-22}$  g was determined from the  $ZrO_2$  molecular weight by multiplying it by the atomic weight unit and the number of LJ centers in the corresponding pillar. The specific volume of molecular complexes in galleries  $V_f$  in the 3rd columns of Tables 5–7 was determined by dividing the weight fraction of pillars  $X$  by the density  $\rho_{pp}$ . Using the calculated values of  $V_{mg}$  and  $V_f$  as well as  $V_{0\Sigma}$  values from Table 1 and the second equation in (5), we calculated the ordering degree of each of the three PIMs for each of the four pillars (see columns 10 in Tables 5–7). Now using the first equation in (5) we found the specific surface areas of galleries  $A_0$  (in the ordered part of the PIM) with all pillars mentally removed from them (see columns 5 in Tables 5–7). Specific areas of side  $A_+$  and base  $A_-$  surfaces of molecular complexes were calculated by multiplying the data from columns 5–7 and 8–10 in Table 4, correspondingly, by the number of pillars in one gram of PIM:  $X/M_{pp}$ .  $A_{mic}$  values in Tables 5–7 mean the total surface area of the interlayer galleries:<sup>10</sup>

$$A_{mic} = A_0 + A_+ - A_-$$

However, this parameter is hardly of any practical interest in our case due to the two-dimensional filling of the galleries. More interesting is the specific surface area  $A_{meas} = A_0 - A_-$  in the 7th columns of Tables 5–7 or even one-half of this value because these characteristics give a more comprehensible impression about the size of the adsorbate monolayer in the galleries per one gram of a sample. It is interesting that for all samples studied here the model complex  $Zr4(2)$  yields the highest values of  $A_{meas}/2$ . Therefore this pillar may be considered as the most suitable from the adsorption and/or catalytic point of view. Comparing  $A_{meas}/2$  for different pillars, note that the following double inequality is true for each sample:

$$A_{BET} - A_{ext} < A_{meas}/2 < A_{BET}$$

Specific values of  $A_{BET}$  and  $A_{ext}$  for each sample can be found in Table 1. So far, it is difficult to attribute certain physical meaning to this observation. Nevertheless, its further testing for other PIMs is of certain practical interest for fast evaluation of  $A_{meas}$ . One more observation useful for interpretation of the adsorption isotherms results from the comparison of specific surface areas  $A_{meas} + A_{ext}$  and  $A_{mic} + A_{ext}$  with the specific surface area  $A_{as}$  from column 8 in Table 1. The last value, which is often believed to have the meaning of the total specific surface area of micropores and mesopores, is in all studied cases much higher than  $A_{meas} + A_{ext}$  or even  $A_{mic} + A_{ext}$ .

Columns 11 in Tables 5–7 present the values of bulk porosity,  $\epsilon_v = V_{mg}/V_0$ , as well as two-dimensional porosity  $\epsilon_a A_{meas}/A_0$ . In some earlier papers,<sup>10</sup> these values were equated because they are identical for model pillars in the form of cylindrical columns. As one can see from the comparative analysis of these two parameters, they are relatively close to each other only for large complexes  $Zr8(1)$  and  $Zr8(2)$ . Columns 12 in Tables 5–7 present the values of effective diameters

$$d_{pv} = [4V_{pc}/\pi H_p]^{0.5} \quad \text{and} \quad d_{ps} = [2A_{bot}/\pi]^{0.5}$$

The first of them is found from the formula for the volume of a circular cylinder. Meanwhile, the second one does not take into account the volume and height. It is obtained from interpretation of the surface occupied by pillars on the pore walls

as two circles. A comparative analysis of columns 12 shows that these two diameters are practically identical for all pillars and all three samples. This result seems paradoxical if one looks at the geometrical shapes of the complexes (Figures 2–4). It is a consequence of the monolayer filling of the narrow interlayer galleries studied by us. Note that in comparison with these effective diameters, the variable corresponding to quadruple pillar volume divided by the surface area of the base has unreasonably large values of about 3 nm for all studied cases. This phenomenon is explained by the specifics of the monolayer gallery filling and the method suggested for calculation of the effective volume and, especially, side surface area of pillars.

Finally, the last columns in Tables 5–7 report the values of the effective distance between the imaginary cylindrical effective surfaces of pillars

$$d_{ipv} = d_{pv}[0.952/(1 - \epsilon_v)^{0.5} - 1] \quad (7)$$

and the effective distance between the imaginary circular bases of the same PP:

$$d_{ipa} = d_{pa}[0.952/(1 - \epsilon_a)^{0.5} - 1] \quad (8)$$

These values are obtained in the assumption of a regular hexagonal arrangement of pillars in the gallery space.<sup>10</sup> They are very close to each other in the cases of large complexes  $Zr8(1)$  and  $Zr8(2)$ . This appears to be quite natural taking into account eqs 7 and 8 and the proximity of  $d_{pv}$  and  $d_{pa}$  values. However, for smaller complexes  $Zr4(1)$  and  $Zr4(2)$  these two effective distances differ approximately by a factor of 2–3. This nonobvious result is caused by the imperfection of the suggested method for determination of the surface area of pillar bases and a high sensitivity of  $d_{ipa}$  and  $d_{ipv}$  values to variation of  $\epsilon_a$  and  $\epsilon_v$  values, respectively, when they are relatively close to 1. Indeed, we determined the area of pillar bases as the number of molecules displaced by the molecular complexes from the near-wall volumes with  $d_{ff}$  thickness (see above). If the width of these volumes is slightly decreased, say, to  $\sigma_{ff}$  or  $\sigma_{sf}$ , the surface area of  $Zr4(1)$  and  $Zr4(2)$  bases is changed enough to alter porosity  $\epsilon_a$  by 0.10–0.15.

Analyzing the obtained PIM characteristics reported in each of Tables 5–7, it is easy to conclude that all of them have quite reasonable values for each of the four model pillars, although in many cases similar characteristics significantly differ for different complexes. Then, 12 additional GCMC simulations were performed to find out for which model pillars the obtained adsorption data correspond better. They gave 12 adsorption isotherms for slitlike pores with the widths 0.8, 0.83, and 0.93 nm containing the required weight fraction of each considered molecular complex: 0.2, 0.195, and 0.206, correspondingly (see columns 2 and 3 of Table 1).

To determine the number of pillars corresponding to an experimental fraction  $X$  with a sufficient precision, the base area of the simulation box was increased to ca.  $20\sigma_{ff} \times 20\sigma_{ff}$  in comparison with the above GCMC simulations on the determination of pillar volumes and surface areas. The lateral coordinates of the pillar centers and directional cosines of their axes were chosen using a random number generator, provided that the distances between the LJ centers in adjacent pillars were at least 0.65 nm. This distance provides a high probability for passing the nitrogen molecules between them. Note that the  $Zr8(2)$  seeding procedure for sample S3(Ba) with the maximum weight concentration of pillars required no less than 1000 initiations of the random number generator and about  $10^6$ – $10^7$  MC trials with a successfully chosen initiation. The total number



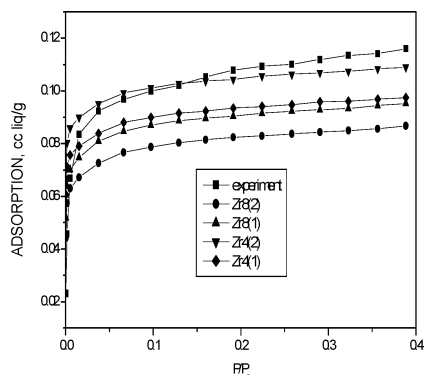


**Figure 5.** Nitrogen adsorption isotherms at 77 K for the S1(Ca) sample: squares, experimental data; circles, GCMC for Zr8(2); up triangles, GCMC for Zr8(1); down triangles, GCMC for Zr4(2); diamonds, GCMC for Zr4(1).

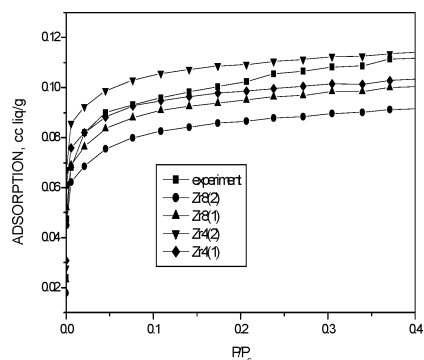


**Figure 6.** Nitrogen adsorption isotherms at 77 K for the S2(Sr) sample: squares, experimental data; circles, GCMC for Zr8(2); up triangles, GCMC for Zr8(1); down triangles, GCMC for Zr4(2); diamonds, GCMC for Zr4(1).

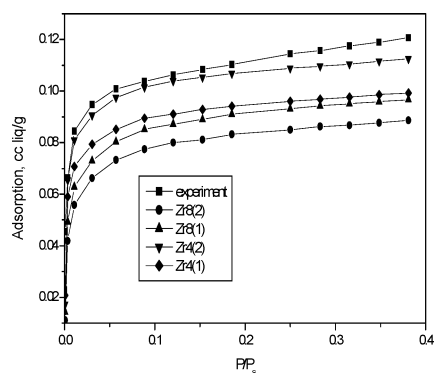


**Figure 7.** Nitrogen adsorption isotherms at 77 K for the S3(Ba) sample: squares, experimental data; circles, GCMC for Zr8(2); up triangles, GCMC for Zr8(1); down triangles, GCMC for Zr4(2); diamonds, GCMC for Zr4(1).

of MC trials for each pillar configuration was equal to  $6 \times 10^7$ . Among them,  $10^7$  trials were made to reach thermodynamic equilibrium, and  $5 \times 10^7$  trials were made to determine adsorption values averaged by the grand canonical ensemble.

The calculated GCMC isotherms of nitrogen adsorption at 77.4 K are shown in Figures 5–7 together with the corresponding experimental isotherms. First, note that for samples S1(Ca) and S3(Ba) the GCMC adsorption isotherms for Zr4(2) are very close to the experimental isotherms at  $P/P_s < 0.2$ , whereas the isotherms calculated for other model pillars pass significantly below the experimental ones. A small upward deviation of the experimental isotherms in comparison with the GCMC isotherms will be discussed below. The relative proximity of the isotherms

for Zr4(2) suggests that only (ZrO<sub>2</sub>)<sub>4</sub> tetramers remain after the final thermal treatment in the interlayer galleries in PIM samples S1(Ca) and S3(Ba) prepared by using pillaring species synthesized via aging of zirconyl chloride solutions containing as additives chlorides of Ca and Ba, respectively, whereas larger complexes are decomposed to these tetramers. In the meantime, the relative proximity of the experimental isotherms to the isotherms calculated for Zr4(2) indicates that, most likely, only two vertexes of tetramers “contact” the gallery walls (see Zr4(2) in Figure 2). The structural reason for such arrangement can be associated with participation of point defects (anion vacancies) in aluminosilicate layers in anchoring of pillaring species. Since random distribution of these defects is affected, this makes less probable their correlated pairwise distribution in the layers required for binding of two vertexes of each tetramer side with the same aluminosilicate sheet.

The comparative analysis of the experimental data and corresponding GCMC isotherms for the S2(Sr) sample appears to be more ambiguous (Figure 6). On one hand, the experimental data satisfactorily match the simulation data obtained for Zr4(1). On the other hand, it is not clear why the tetramers would prefer the orientation rotated by 45° in comparison with samples S1(Ca) and S3(Ba). In this case simultaneous filling of the galleries with complexes Zr4(2) and Zr8(1) appears to be more likely. Indeed, the GCMC isotherm calculated using 62 wt % Zr8(1) and 38 wt % Zr4(2) is indistinguishable from the one corresponding to the gallery filling with Zr4(1) complexes alone (diamonds in Figure 6). These special GCMC calculations for the S2(Sr) sample give us the ability to characterize the final pore structure of all three samples studied. Columns 2–13 of Table 8 are organized as analogous columns in Tables 5–7. However the first column contains the acronyms of samples. The S1(Ca) and S3(Ba) lines of Table 8, of course, are identical to the Zr4(2) lines of Table 5 and Table 7, respectively, while the pore structure characteristics in the S2(Sr) row of Table 8 were calculated using the ratio of different complexes (38 wt % Zr4(2)/62 wt % Zr8(1)) found for the S2(Sr) sample.

Thus, it may be concluded that the presence of Sr cations in the pillaring zirconyl chloride solution, most likely, promotes the formation of sheet-type pillaring species preserving their geometrical structure in the montmorillonite galleries after removal of Sr by washing followed by calcination. This means simultaneously that adsorption and/or catalytic properties of supports, prepared by using pillaring species synthesized via aging of zirconyl chloride solutions containing as additives chloride of Sr, should be worse than those of supports prepared with use of solutions containing Ca or Ba cations (see the values of  $A_{\text{meas}}$  and  $d_{\text{ipv}}$  in Table 8).

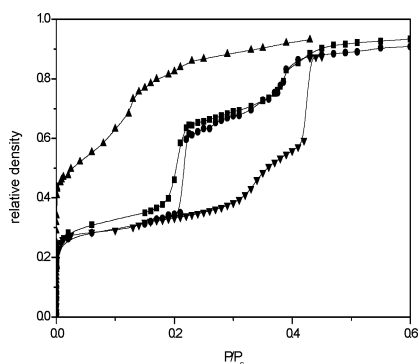
At the end of this section, we clarify the problem with the steeper slope of the experimental isotherms in comparison with those simulated by GCMC at  $P/P_s > 0.2$ . We believe that this phenomenon is caused by the accumulation of excessive adsorbate at the joints of lamellar montmorillonite blocks and in places where the integrity of layers forming the gallery walls is broken. To illustrate our hypothesis, we have simulated adsorption in “double” galleries, i.e., micropores with ca. 2.8 nm height resulting from the removal of a part of one montmorillonite layer and having different widths. Figure 8 presents four GCMC nitrogen adsorption isotherms for 4 capillaries with rectangular sections of the above height and different widths. It was assumed that all four capillary walls had the same potential parameters (see Table 2) and the energy of interaction with them could be calculated using the corresponding Bojan–Steele potential.<sup>33</sup> Hereafter all dimensions will

TABLE 8: Calculated S1(Ca), S2(Sr), and S3(Ba) Data

sample	$V_{mg}$ , cm <sup>3</sup> /g	$V_f$ , cm <sup>3</sup> /g	$V_0$ , cm <sup>3</sup> /g	$A_0$ , m <sup>2</sup> /g	$A_+$ , $A_-$ , m <sup>2</sup> /g	$A_{meas}$ , m <sup>2</sup> /g	$A_{mic}$ , m <sup>2</sup> /g	$\rho_{pp}$ , g/cm <sup>3</sup>	$z$	$\epsilon_v$ , $\epsilon_a$	$d_{pv}$ , $d_{pa}$ , nm	$d_{ipv}$ , $d_{ipa}$ , nm
S1(Ca)	0.173	0.071	0.244	533	59, 44	489	547	2.82	0.96	0.71, 0.92	0.680, 0.680	0.520, 1.564
S2(Sr)	0.144	0.060	0.205	416	90, 76	325	434	3.41	0.77	0.71, 0.78	0.763, 0.762	0.602, 0.891
S3(Ba)	0.188	0.097	0.286	523	57, 48	474	532	2.11	0.97	0.66, 0.91	0.728, 0.696	0.459, 1.493

be reported in LJ diameters of nitrogen. The topmost isotherm in Figure 8 was calculated for a capillary with a  $7 \times 7$  square section. Its shape resembles experimental isotherms typical for microporous materials because most of the nitrogen is adsorbed at relatively low pressures. Note that the ordinate axis of the graph contains relative adsorbate densities, i.e., the numbers of molecule centers in a cube with the side equal to  $\sigma_{ff}$ . During the corresponding GCMC experiment, it was found that a very significant fraction of the adsorbate was adsorbed at the corners of the  $7 \times 7$  pore already at  $P/P_s < 5 \times 10^{-4}$ . When the pressure increased, the adsorbate surface became looser and more fluctuating. In the relative pressure range of ca.  $5 \times 10^{-2} < P/P_s < 0.1$ , the “gas” part of the pore volume was already filled with a loose condensate rather than with a dense vapor. Its density varied between 15 and 40% of the normal liquid density. Such a behavior of the adsorbate is typical for classic Dubinin *bulk filling* of micropores, although, according to the IUPAC classification, 28 Å pores belong to mesopores. If such small structural defects of the montmorillonite layers were present in real PIM in significant amounts, this would make the analysis of their pore structure more complex. Fortunately, it seems that the share of such defects in the total pore volume of PIM is insignificant, at least for samples S1(Ca), S2(Sr), and S3(Ba).

The lower GCMC isotherm in Figure 8 is the extreme theoretical case when a “double gallery” has unlimited length in the lateral directions. The lack of the side walls (and, consequently, corners) prevents meniscus-like accumulation of adsorbate in the pore corners and its filling at low  $P/P_s$ . Gradual filling of the pore occurs at  $P/P_s < 0.45$  by growth of the adsorption film at the top and bottom walls. At  $P/P_s \sim 0.45$ , these films approach each other close enough ( $\sim 3\text{--}3.5\sigma_{ff}$ ) for the decreased potential of the space between the films to initiate spontaneous vapor condensation at the film surface and, thus, filling of this space with the condensate. Note that this is the filling mechanism of slitlike pores considered in the modern nonlocal density functional theory,<sup>34</sup> which forms the bases for corresponding routine calculations of the pore size distributions. Among real layered materials, this mechanism is, apparently, very rare and does not contribute substantially to the total volume of the adsorbate during investigation of real porous materials. Indeed, such filling can take place only between two



**Figure 8.** Isotherms of nitrogen adsorption at 77.4 K in a slitlike pore with the height  $7\sigma_{ff}$  and in rectangular pores with the same height and different widths: down triangles, slitlike pore; up triangles,  $7 \times 7$  pore; squares,  $7 \times 120$  pore; circles,  $7 \times \infty$  pore.

relatively extended flat ledges on the walls of a larger pore. Such situation appears to be very unlikely.

The two remaining isotherms in Figure 8 correspond to adsorption in a  $7 \times 120$  rectangular capillary. Squares mark the density growth in the whole accessible capillary volume. Circles mark the density calculated only in the central  $7 \times 7 \times 7$  part of the capillary. In other words, in the latter case the contribution of additional condensate in the pore corners is excluded, and the corresponding isotherm can be interpreted as filling of a rectangular capillary of arbitrarily large width. Comparison of the last two GCMC isotherms indicates that the  $7 \times 120$  model capillary with the width ca. 17 times larger than its height still yields a substantial contribution of additional condensate appearing in the pore corners, especially before the pore filling at about  $P/P_s = 0.2$ . Obviously, if adsorption isotherms were calculated for pores with height equal to 7 and width in the range of 7–120, they would lie in a wide space between the two top isotherms in Figure 8.

The considered example encourages the idea that a fairly wide selection of GCMC isotherms calculated in double galleries together with the isotherm on an open surface and a set of isotherms in interlayer micropores containing various molecular complexes could become the basis for a database for solution of the corresponding adsorption integral with the goal of more detailed and reliable characterization of the PIM pore structure.

## Summary

Four models of molecular complexes  $(ZrO_2)_n$  in the interlayer micropores of montmorillonite are suggested. GCMC simulation of nitrogen adsorption has been carried out to determine effective molecular geometrical characteristics of these complexes. They were used to determine the parameters of the pore structure of three supports for catalysts, which are used for reduction of nitrogen oxides with hydrocarbons, in the frames of the partially disordered PIM model.<sup>10</sup> The use of either of the suggested model zirconium dioxide complexes was found to yield reasonable pore structure characteristics. Therefore, additional numerical experiments were carried out. They allowed us to compare the experimental adsorption isotherms of the studied samples with the GCMC isotherms corresponding to different  $(ZrO_2)_n$  complexes. Comparison of the experimental and model isotherms led us to the conclusion that only the simplest  $(ZrO_2)_4$  tetramers are, most likely, present in the samples of catalysts prepared by using pillaring species synthesized via aging of zirconyl chloride solutions containing as additions Ca and Ba chlorides. In the case of samples prepared by using a pillaring solution containing Sr cations, besides the simplest tetramers, a significant amount of more complex sheetlike complexes  $(ZrO_2)_8$  are present in the interlayer micropores.

**Acknowledgment.** This work is in part supported by Integration Project 8.23 of Presidium RAS. We thank Dr. V. A. Drozdov for providing a part of the adsorption experimental data.

## References and Notes

- (1) Burch, R.; Warburton, C. I. *J. Catal.* **1986**, *97*, 503.
- (2) Gil, A.; Gandia, L. M. *Catal. Rev.—Sci. Eng.* **2000**, *42*, 146.



- (3) Yang, R. T.; Trappiwattanannon, N.; Long, R. Q. *Appl. Catal. B* **1998**, *19*, 289.
- (4) Konin, G. A.; Il'ichev, A. N.; Matushak, V. A.; Khomenko, T. I.; Korchak, V. N.; Sadykov, V. A.; Doronin, V. P.; Bunina, R. V.; Alikina, G. M.; Kuznetsova, T. G.; Paukshtis, E. A.; Fenelonov, V. B.; Zaikovskii, V. I.; Ivanova, A. S.; Beloshapkin, S. A.; Rozovskii, A. Ya.; Tretyakov, V. F.; Ross, J. R. H.; Breen, J. P. *Top. Catal.* **2001**, *17*, 193.
- (5) Sadykov, V. A.; Bunina, R. V.; Alikina, G. M.; Doronin, V. P.; Sorokina, T. P.; Kochubei, D. I.; Novgorodov, B. N.; Paukshtis, E. A.; Fenelonov, V. B.; Derevyankin, Yu.; Ivanova, A. S.; Zaikovskii, V. I.; Kuznetsova, T. G.; Beloshapkin, S. A.; Kolomiichuk, V. N.; Plyasova, L. M.; Matyshak, V. M.; Konin, G. A.; Rozovskii, A. Ya.; Tretyakov, V. F.; Burdeynaya, T. N.; Davydova, M. N.; Ross, J. R. H.; Breen, J. P.; Meunier, F. C. *Mater. Res. Soc. Symp. Proc.* **2000**, *581*, 435.
- (6) Sadykov, V. A.; Kuznetsova, T. G.; Doronin, V. P.; Sorokina, T. P.; Alikina, G. M.; Kochubei, D. I.; Novgorodov, B. N.; Paukshtis, E. A.; Fenelonov, V. B.; Zaikovskii, V. I.; Rogov, V. A.; Anufrienko, V. F.; Vasenin, N. T.; Matyshak, V. A.; Konin, G. A.; Rozovskii, A. Ya.; Tretyakov, V. F.; Burdeynaya, T. N.; Ross, J. P. R.; Breen, J. P. *Chem. Sustainable Dev.* **2003**, *11*, 249.
- (7) Yang, R. T.; Baksh, M. S. A. *AIChE J.* **1991**, *37*, 679.
- (8) Baksh, M. S. A.; Kikkinides, E. S.; Yang, R. T. *Ind. Res. Chem. Res.* **1992**, *31*, 2181.
- (9) Baksh, M. S. A.; Yang, R. T. *AIChE J.* **1992**, *38*, 357.
- (10) Fenelonov, V. B.; Derevyankin, A. Ya.; Sadykov, V. A. *Microporous Mesoporous Mater.* **2001**, *47*, 359.
- (11) Occeli, M. I.; Bertand, J. A.; Gould, S. A. C.; Dominguez, J. M. *Microporous Mesoporous Mater.* **2000**, *34*, 195.
- (12) Nijs, H.; De Bock, M.; Maes, N.; Vansant, E. F. *J. Porous Mater.* **1999**, *6*, 307.
- (13) Cao, D.; Wang, W. *Phys. Chem. Chem. Phys.* **2001**, *3*, 3150.
- (14) Cao, D.; Wang, W.; Duan, X. *J. Colloid Interface Sci.* **2002**, *254*, 1.
- (15) Yi, X.; Shing, K. S.; Sahimi, M. *Chem. Eng. Sci.* **1996**, *51*, 3409.
- (16) Ghassemzadeh, J.; Xu, L.; Tsotsis, T. T.; Sahimi, M. *J. Phys. Chem. B* **2000**, *104*, 3892.
- (17) Sadykov, V. A.; Kuznetsova, T. G.; Doronin, V. P.; Sorokina, T. P.; Kochubei, D. I.; Novgorodov, B. N.; Kolomiichuk, V. N.; Moroz, E. M.; Zyuzin, D. A.; Paukshtis, E. A.; Fenelonov, V. B.; Derevyankin, A. Ya.; Beloshapkin, S. A.; Matyshak, V. A.; Konin, G. A.; Ross, J. P. R. *Mater. Res. Soc. Symp. Proc. Ser.* **2002**, *703*, 529.
- (18) Carrusers, J. D.; Cutting, P. A.; Day, R. E.; Harris, M. R.; Mitchell, S. A.; Sing, K. S. W. *Chem. Ind.* **1968**, 1772.
- (19) Setoyama, N.; Suzuki, T.; Kaneko, K. *Carbon* **1998**, *36*, 1459.
- (20) Miehe-Brendle, J.; Khouchaf, L.; Baron, J.; Le Dred, R.; Tuilier, M.-H. *Microporous Mater.* **1997**, *11*, 171.
- (21) Singhal, A.; Toth, L. M.; Lin, J. S.; Affholter, K. *J. Am. Chem. Soc.* **1996**, *118*, 11529.
- (22) Hu, M. Z.-C.; Zielke, J.; Lin, J.-S.; Byers, Ch. H. *J. Mater. Res.* **1999**, *14*, 103.
- (23) Sadykov, V. A.; Kuznetsova, T. G.; Doronin, V. P.; Moroz, E. M.; Zyuzin, D. A.; Kochubei, D. I.; Novgorodov, B. N.; Kolomiichuk, V. N.; Alikina, G. M.; Bunina, R. V.; Paukshtis, E. A.; Fenelonov, V. B.; Lapina, O. B.; Yudaev, I. V.; Mezentseva, N. V.; Volodin, A. M.; Matyshak, V. A.; Lumin, V. V.; Rozovskii, A. Ya.; Tretyakov, V. F.; Burdeynaya, T. N.; Ross, J. R. H. *Top. Catal.* **2005**, *32*, 29.
- (24) Bartley, G. J. J. In *Catalysis Today*, 2; Burch, R., Ed.; Elsevier: Amsterdam, 1988; p 233.
- (25) Jiang, S.; Rhykerd, C. I.; Gubbins, K. E. *Mol. Phys.* **1993**, *79*, 273.
- (26) Steele, W. A. *The interaction of gases with solid surfaces*; Pergamon: New York, 1974.
- (27) Hirschfelder, J. O.; Curtis, C. E.; Bird, R. B. *Molecular Theory of Gases and Liquids*; J. Wiley & Sons: New York, 1954.
- (28) Nicholson, D.; Parsonage, N. G. *Computer Simulation and the Statistical Mechanics of Adsorption*; Academic Press: London, 1982.
- (29) Jacobsen, R. T.; Stewart, R. B.; Jahangiri, M. J. *J. Phys. Chem. Ref. Data* **1968**, *15*, 735.
- (30) Adams, D. J. *Mol. Phys.* **1976**, *32*, 647.
- (31) Rowley, L. A.; Nicholson, D.; Parsonage, N. G. *J. Comput. Phys.* **1975**, *17*, 401.
- (32) Barker, J. A.; Monaghan, J. J. *Chem. Phys.* **1962**, *36*, 2564.
- (33) Bojan, M. J.; Steele, W. A. *Carbon* **1998**, *36*, 1417.
- (34) Lastoskie, C.; Gubbins, K. E.; Quirk, N. J. *J. Phys. Chem.* **1993**, *97*, 4786.